Available online at www.sciencedirect.com

ScienceDirect

Advances in Space Research xx (2021) xxx-xxx

ADVANCES IN SPACE RESEARCH (a COSPAR publication)

www.elsevier.com/locate/asr

Identifying illumination conditions most suitable for attitude detection in light curves of simple geometries

Laurence Blacketer[a,*], Hugh Lewis[a], Hodei Urrutxua[b]

[a] Astronautics Research Group, The University of Southampton, Southampton SO17 1BJ, UK
[b] Aerospace Systems and Transport Research Group, Universidad Rey Juan Carlos, Madrid, Spain

Abstract

The objective of this paper is to identify the illumination conditions that maximise the differences that can be measured between light curves of an object resulting from its attitude state. This is relevant to attitude determination techniques using light curve data, and is valuable for the design of observation strategies that maximise the information contained in light curves.

For this purpose, synthetic light curves were generated for a number of attitude states, object geometries and illumination configurations. The light curves were generated through application of a Bidirectional Reflectance Distribution Function (BRDF) to a faceted object geometry. The differences between the light curves were quantified using a Root Mean Square Error (RMSE).

Results showed that, depending on the reflection model, the object geometry and the attitude state, particular illumination conditions existed that led to the largest RMSE between different attitude states. In most cases, increasing the phase angle increased the RMSE between light curves arising from different attitude states. The maximum RMSE occurred when the illumination vector was either aligned with the rotation vector or offset from it by 90°. It is concluded that characterising the rotational motion of an object from its brightness data is best performed using multiple observations. These observations should be constructed in a way that maximises the difference in the illumination geometry. One way of achieving this would be to use observations from multiple observatories with a diverse range of geographical locations.

Keywords: Space debris; Optical ; Light curves; Simulation; Attitude determination

1. Introduction

Near-Earth space has become one of humanity's most valuable resources. Many aspects of modern-day life now rely upon our satellite infrastructure. However, more than 70 years of space flight have left large amounts of space debris within this environment. As of January 2020 there were more than 20000 Resident Space Objects (RSOs) that could be reliably tracked using ground-based radars and telescopes (object diameter >10 cm) (Liou et al., 2020). These RSOs range from small mission-related debris such as lens-caps, up to the massive upper stages of rockets. This number increases by orders of magnitude when small objects that cannot be reliably tracked are included. Their presence is known through occasional observations or inferred through statistical analysis (Schildknecht, 2007).

The large number of RSOs in near-Earth space has raised concerns that Earth's orbital environment is not being used sustainably. Evolutionary debris models have been used to help explore this issue. Results indicate that the number of objects in Earth-orbit may already be sufficient to sustain orbital pop-

*Corresponding author: Tel.: +0-000-000-0000; fax: +0-000-000-0000;
Email address: ldjb1g15@soton.ac.uk (Laurence Blacketer)

https://dx.doi.org/10.1016/j.jasr.xxxx.xx.xxx

ulation growth through collision activity, even without future launch traffic (Liou & Johnson, 2008; Lewis et al., 2009). One of the suggested solutions is Active Debris Removal (ADR), where a massive object with high risk of involvement in future collision activity is removed from the space environment (Lewis et al., 2009; Liou & Johnson, 2009).

In addition to the goal of space sustainability, spacecraft operators want to ensure that their mission remains safe from impacts with space debris. This is particularly the case for high-value orbits such as Sun-synchronous and Geosynchronous. For these reasons, Collision Avoidance (CA) has become a critical component of modern space operations.

ADR and CA analysis both require highly accurate data on object position and attitude state. Powerful radar installations are capable of providing this information, but their high cost precludes them from being more generally applicable to the entire RSO population. However, low-cost optical systems can be deployed in large numbers across the globe and provide an attractive alternative. Although, simple, low-cost optical systems are only capable of measuring object brightness against time, these light curves can be collected in very large numbers. As a result, light curves may form an important component of future Space Situational Awareness (SSA) capabilities.

Optical light curves have a long heritage in determining properties such as rotation period (Goguen et al., 1976), shape, albedo and attitude (Kaasalainen et al., 1992b,a) of asteroids (Kaasalainen & Torppa, 2001; Kaasalainen et al., 2001; Torppa et al., 2003), using a variety of techniques. Determination of each of these properties is performed using a priori information for the others, either assumed or determined using other techniques.

Light curves have also been used to determine various properties of spacecraft. For instance, light curves of tumbling spacecraft typically exhibit highly periodic signals and so have proved to be well-suited for determining rotation rates through periodicity analysis (Šilha et al., 2018). Performing this periodicity analysis over time has been used to determine rotation rate dynamics and provide insight into the on-orbit torques that induce this rotational motion (Earl & Wade, 2015). Attempts have been made to use light curve analysis to determine the direction of the rotation vector (Williams, 1979a,b), and have also been applied over time to determine the evolution of rotational dynamics (Koshkin et al., 2016). Techniques are also being developed to use light curves for object shape characterisation (Linares et al., 2014).

Determination of space object rotation state is of particular importance for ADR and CA analysis. For CA, attitude state information can be used to calculate forces such as atmospheric drag and solar radiation pressure more accurately, reducing the uncertainty in a predicted future position. Minimising the uncertainty in position predictions provides higher confidence in determining if an operator should move their satellite to avoid a collision. For ADR, if the mission needs to capture an object, such as with a robotic arm, then the attitude state must be well characterised. Studies have shown the viability of light curve attitude state determination, (Wetterer & Jah, 2009), but further research is required in order to fully understand the relationship between attitude state and brightness signal. This paper contributes by examining the observability and measurability of the rotational state, as a function of the illumination and observation geometry.

The objective of this work was to identify illumination conditions under which the light curves of an object with different attitude states are most different from one another. This will help to devise observation strategies that maximise the likelihood that an object is observed in a way that its rotational motion is detectable and distinguishable from similar rotational motions. Additionally, it will help to identify and avoid illumination conditions that are not well suited for detecting or distinguishing rotational motion. To achieve this objective, synthetic light curves were generated for a selection of object geometries and rotational motions and the illumination conditions under which they were most different were identified. It is not possible to test all combinations of object geometry, attitude state and illumination conditions. These three properties were therefore constrained to a small range of representative examples.

Three object geometries were selected. These were: a cube, a 20-sided icosahedron and a 500-sided polyhedron. The cube geometry was selected as it is a good analogue of the typical 'box-like' shape of a satellite. The icosahedron was selected because it has facets at a range of different angles, which is representative of satellites that have less uniform surfaces. Finally, the polyhedron geometry was used to be representative of a sphere. Although spherical objects are much rarer in Earth orbit, in theory their rotational motions should be the least detectable and distinguishable. The polyhedron was therefore included as a control.

The rotational motions considered in this paper were constrained to rotations about an axis that remained fixed in inertial space. In order to measure differences between different rotations, three rotation vectors were selected. These were rotations about each of the three orthogonal body-fixed axes. In addition, a 'no-rotation case' was included as a control.

Finally, a range of illumination conditions were required. This was achieved by fixing the direction of the observation vector to be coincident with one of the three body-fixed orthogonal axes, then varying the direction of the illumination vector. Differences between light curves were quantified using Root Mean Square Error (RMSE). Light curves generated with various combinations of object geometry, rotational motion and illumination conditions were compared first using a purely diffuse reflection model, then again using a purely specular model of reflection.

This paper is organised as follows: Section 2 describes the model used to generate synthetic light curves, including a description of the reference frame and model inputs. Section 3 provides the numerical results simulating various illumination and rotation conditions, together with the key discussion points. The results for selected illumination conditions are presented, then the results and discussion are extended to a realistic light curve scenario. This demonstrates some of the key findings and their relevance to real-life applications. The final conclusions are summarised in Section 4.

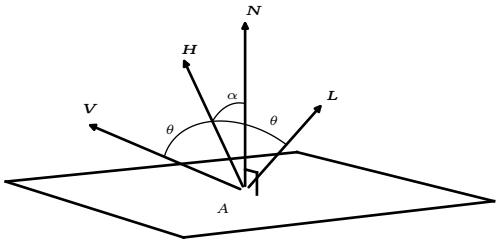

Fig. 1. The reflection geometry. **V** is the observation vector, **L** is the illumination vector and **H** is the angular bisector of these two vectors. **N** is the surface normal and A is the surface area. The angle between **V** and **L** is 2θ and the angle between **H** and **N** is α.

2. Methodology

To generate a synthetic brightness measurement, a Bidirectional Reflectance Distribution Function (BRDF) was applied to every facet of a geometry model. A BRDF calculates the light reflected from a surface in a given direction due to illumination from another direction. Summing the brightness contributions from each face of the geometry model, at each time step, allows the production of a synthetic light curve as observed from a prescribed direction.

The apparent magnitude of an object $m_{1,\text{app}}$, relative to an object $m_{2,\text{app}}$, is calculated using the equation

$$m_{1,\text{app}} = m_{2,\text{app}} - 2.5 \log_{10}\left(\frac{B_1}{B_2}\right) \tag{1}$$

where B_1 and B_2 are the measured fluxes of objects 1 and 2 respectively (Kutner, 2003). The Cook-Torrence BRDF is given by

$$C_i = (sR_s + dR_d)\pi A_i(\mathbf{N}_i \cdot \mathbf{L})(\mathbf{N}_i \cdot \mathbf{V}), \tag{2}$$

where C_i is the ratio of incident to reflected flux at the i-th facet, A_i is the area of the i-th facet, R_s and R_d are the specular and diffuse bidirectional reflectances and s and d are the specular and diffuse coefficients, with $s+d = 1$ (Cook & Torrance, 1982). The surface normal vector, $\mathbf{N}_i$, illumination vector, **L**, and the observation vector, **V**, are shown in Fig 1.

The diffuse and specular reflectances are given by the equations

$$R_d = \frac{\omega}{\pi} \tag{3}$$

and

$$R_s = \frac{F}{\pi}\frac{DG}{(\mathbf{N}\cdot\mathbf{L})(\mathbf{N}\cdot\mathbf{V})}, \tag{4}$$

where ω is the diffuse albedo. F and G and are the surface reflectance and geometric attenuation factor, respectively. Further information on the calculation of F and G is available in Ref. (Cook & Torrance, 1982). The property D is the facet slope function, which provides the fraction of facets that are aligned with the angular bisector vector, **H**. **H** is the normal vector of a hypothetical surface for which the angle of incidence is equal to the angle of reflection, leading to specular reflection. D is a function of α, the angle between the angular bisector and surface normal vectors, and a Root Mean Square (RMS) slope term, m, which parameterises the surface roughness. Higher values for m correspond to a rougher surface and hence a broader distribution in the specular reflections.

The ratio of incident to reflected flux, C, as seen by an observer at a distance r, and summed across all reflecting surfaces N, is given by

$$C = \sum_{i=1}^{N}\frac{B_i}{4\pi r^2}, \tag{5}$$

(Wetterer & Jah, 2009). As the incident flux is due to the Sun, C is equal to the ratio of B_1 to B_2 in Eq. 1. Eq. 5 can therefore be substituted into Eq. 1, together with the Sun's apparent magnitude to arrive at the equation:

$$m_{\text{app}} = -26.74 - 2.5\ \log_{10}\left(\sum_{i=1}^{N}\frac{B_i}{4\pi r^2}\right). \tag{6}$$

Evaluating this equation at a succession of time steps allows production a synthetic light curve. The synthetic brightness model described above does not accommodate shadowing and occultation of facets, which was unnecessary as all of the considered geometry models are convex.

The difference between two synthetic light curves is quantified with a RMSE, using the equation

$$RMSE = \sqrt{\frac{\sum_{i=1}^{n}(\hat{y}_i - y_i)^2}{n}}, \tag{7}$$

where $\hat{y}_i$ and y_i are the i-th data points of the two light curves, each containing n data points.

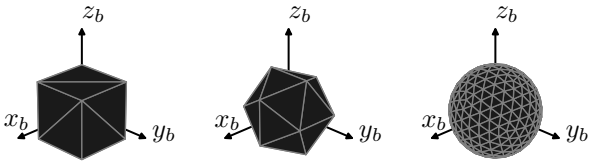

Fig. 2. The three object geometries considered in this paper. A 'b' subscript denotes a body-fixed axis.

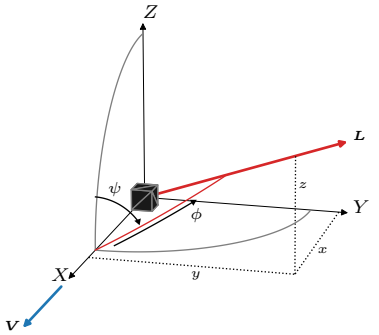

Fig. 3. A figure showing the reflection geometry and object geometry. The observation vector, **V**, is aligned with the X-axis of the system and the position of the illumination vector, **L**, is defined by the angles ψ and ϕ.

The three object geometries are shown in Figure 2. These are: a cube, a 20-sided regular icosahedron, and a polyhedron where each facet of the icosahedron has been subdivided into 25 facets, such that the centroid of each facet is equidistant from the centre of the geometry. The cube has a side-length of 2 m and the icosahedron and polyhedron each have a radius of 1 m.

Figure 3 shows the reflection configuration used in the generation of each synthetic light curve with respect to the prescribed reference frame XYZ. The vector **V** is the observation vector and always remains aligned with the X axis. The vector **L** is the illumination vector, the direction of which is varied to analyse its influence on the generated light curve. The illumination vector is offset from the X axis with a direction described by the two angles ψ and ϕ, where ψ is the angle between the XZ plane and the plane containing the X axis and **L** vector, and ϕ is the angle formed between the X axis and **L** vector. These two angles therefore describe the offset of the illumination vector, **L**, with respect to the observation vector, **V**. ϕ is the angle between the illumination and observation vectors, and is therefore the phase angle.

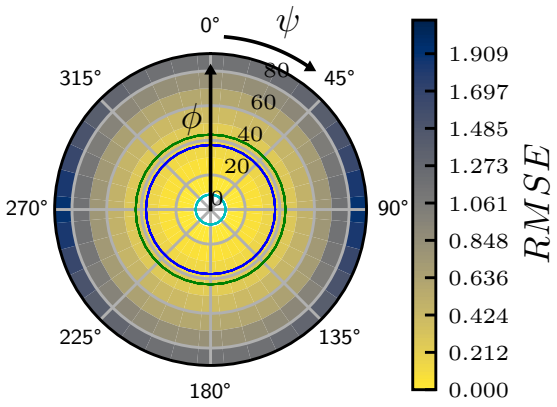

Fig. 4. An example polar plot for the cube geometry with a diffuse reflection and a rotational motion about the Y body-fixed axis.

All synthetic light curves were generated with the object placed at 1000 km from the observer. The position of the object was fixed and was only allowed to rotate about its geometric centre. Each light curve was 240 s long with a 0.1 s time step.

3. Results and Discussion

The results for this work are RMSE measurements between a baseline light curve, which will be discussed later, and a second light curve generated with a different illumination vector direction. Because the direction of the illumination vector is described using the two angles ψ and ϕ, the results are presented in the form of polar plots. An example polar plot is provided as Figure 4, where ψ is measured clockwise along the periphery of the plot and ϕ is measured radially. These polar plots describe the direction of an illumination vector in a hemisphere centred on the direction of the observation vector. The angle ϕ is therefore equivalent to the phase angle. The colour of each pixel shows the RMSE between a light curve generated with an illumination vector direction given by the position on the plot and a baseline light curve. When the colour is white, such as the innermost ring of pixels in Figure 4, the RMSE is zero. These plots were generated for four different rotational motions, either no-rotation, or rotation about one of three body-fixed axes: x_b, y_b and z_b. Initially, the observation vector and the body-fixed x_b axis were coincident with the X axis of Figure 3. Therefore, a rotation about the x_b axis is the same as a rotation about the observation vector. This set of four plots were then generated for each of the three object geometries. This entire process was performed twice, firstly using a purely diffuse reflection model, then again using a purely specular reflection model.

The reference frame in Figure 3 is used to represent a satellite-centred orbital reference frame. In such a frame, and assuming a circular orbit, the Z axis is normal to the orbital plane, the Y axis is aligned with the velocity vector and the X axis points away from the centre of the Earth. Each plot also includes three concentric circles, which indicate the angular region within which the theoretical position of the Earth would obscure these illumination vectors. These three circles correspond to, in order of increasing value of ϕ, orbital altitudes of 35,786 km, 2000 km and 1000 km. In Figure 4 and all subsequent Figures, these three circles are coloured cyan, blue and green respectively. In this work the objects have been set at 1000 km, but these circles illustrate how some illumination vectors would become available as orbital altitude increases.

3.1. Cube with diffuse reflection

The first result is presented as Figure 5, for the cube geometry and a diffuse reflection model. The cube was selected to represent the typical 'box-like' shape of satellites. The baseline light curve, indicated at the centre of the no-rotation plot using a green 'x', corresponds to a non-rotating object with $\phi = \psi = 0$. Within this figure, are the results for the four different rotational motions that were considered. For the three rotating cases, the direction of the rotation axis is indicated using a red '+'. The pixelation of the plots is caused by using 10° bins for ϕ and ψ. Because the geometry being considered is a cube, an illumination vector offset of 90° ($\phi = 90°$) results in no light being reflected in the direction of the observation vector. For this reason, the outermost ring of pixels in each of these polar plots is excluded.

In these plots the RMSE measured against the baseline case increases as phase angle ϕ is increased. This is caused by an overall reduction in light curve brightness that results from an increased phase angle. Considering only the no-rotation and x-rotation cases, the results are identical and independent of ψ.

This is because only a single face of the cube contributes to the reflection, which remains perpendicular to the observation vector throughout the light curve timespan. In the y-rotation and z-rotation cases, the largest RMSEs were measured when the illumination vector was closely aligned with the rotation vector (red '+'s). In all four polar plots, zero RMSE was measured in the innermost ring of pixels that corresponded to $\phi = 0$. This indicates that under such illumination conditions, rotating and non-rotating objects were indistinguishable from each other.

Figure 6 shows the result of performing a pixel-to-pixel subtraction between the polar plots of each of the rotating cases. To correct for negative values, the absolute value of this subtraction was used. These plots remove the effect of brightness reduction due to increased phase angle, allowing the differences between the individual rotational motions to be seen more easily. These plots do not measure the RMSE between the two rotational motions, but rather the difference in the RMSE measured from the baseline for each state. Therefore, zero-valued pixels in this plot do not necessarily show that the light curves of the two different rotational motions are identical, just that the two light curves are different from the baseline by an exactly equal amount. The rotation vectors of the two rotational motions being compared are again indicated using red '+'s. These plots show that the direction of the illumination vector can have a large effect on the difference in RMSE measured between the two light curves and the baseline. Depending upon which two rotational motions are being compared, the largest RMSE differences are recorded either when the illumination vector is aligned with the rotation vector (z-y case), or when the ψ angle of the illumination vector is offset from the ψ angle of the rotation vector by 90° (y-x and z-x cases). In all cases, the largest differences are always measured when the illumination vector is offset from the observation vector by 90°.

These results for the cube geometry highlight the illumination conditions that are most ideal for distinguishing rotational motions. In all cases, a large offset between the observation and illumination vectors is desired. The ideal direction of the illumination with respect to the rotation vector is dependent upon

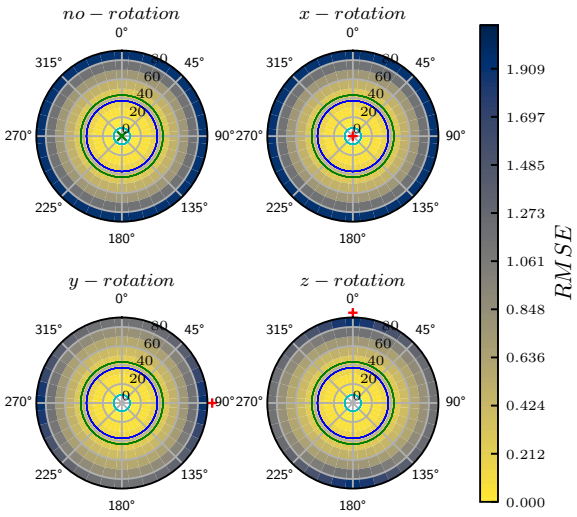

Fig. 5. Results for a diffuse reflection model and a cubic object geometry. RMSE is measured from a no-rotation no illumination offset baseline.

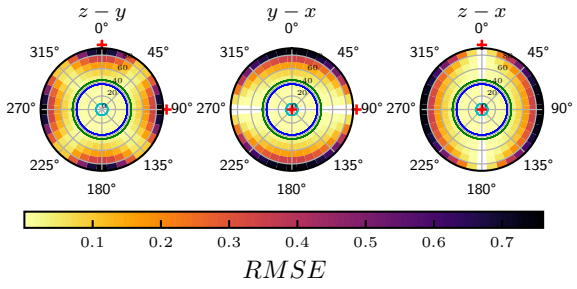

Fig. 6. The result of performing a pixel-to-pixel subtraction between two of the plots from Figure 5. The two rotation cases in question are labelled above each polar plot. The reflection model is diffuse and the object geometry is a cube.

the two rotational motions to be distinguished. In Figure 6, the band of white pixels that are horizontal through the origin in the y-x plot (middle) and vertical in the z-x plot (right) shows that these attitude motions are indistinguishable if the observation vector, the illumination vector and the rotation vector are all in the same plane.

Note that the y-x plot (middle) is exactly the same as the z-x plot (right), but rotated through 90°. This is the case for all of the subtraction results presented in this paper. For this reason, the z-x polar plot is excluded from all subsequent figures.

3.2. Cube with specular reflection

The next result is for the cube geometry with a specular reflection model. All model inputs and parameters are identical to the diffuse results, with the only exception being the reflec-

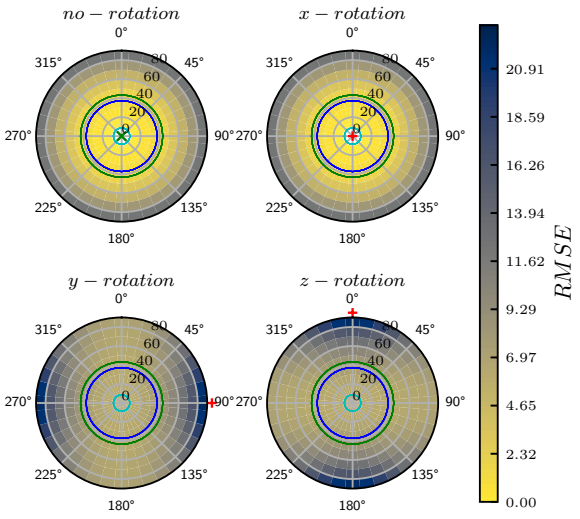

Fig. 7. Results for a specular reflection model and a cubic object geometry. RMSE is measured from a no-rotation no illumination offset baseline.

tion model. Considering Figure 7, the magnitudes of the RMSE measurements are larger than for the diffuse results, but the positions of the largest RMSE values with respect to the illumination and rotation vectors are the same. The most notable difference is that the innermost ring of pixels for $\phi = 0$ in the y-rotation and z-rotation cases no longer correspond with zero RMSE. This shows that with specular reflection these rotational motions can be distinguished, which was impossible under diffuse reflection conditions.

Figure 8 shows the result of the pixel-to-pixel subtraction. The z-y case is the same as for the diffuse reflection model. However, the y-x and z-x cases show an inverted behaviour. The largest RMSE now occurs when the illumination vector is aligned with the rotation vector, rather than when they are offset by 90°.

With specular reflection, the most ideal conditions for distinguishing rotational motions are again with maximum illumination vector offset. The ideal direction for the illumination vector is to be coincident with the rotation axis.

3.3. Icosahedron with diffuse reflection

The next two figures show the results for the icosahedron geometry with a diffuse reflection model. The icosahedron geometry was selected due to it having a more varied range of facet angles. In Figure 9 the y-rotation and z-rotation cases have been

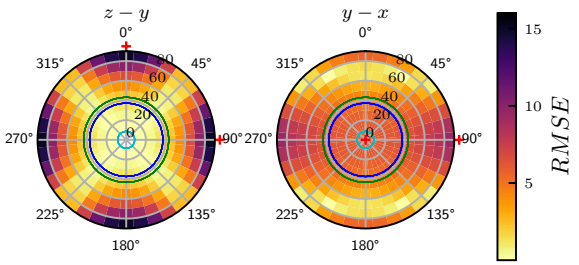

Fig. 8. The result of performing a pixel-to-pixel subtraction between two of the plots from Figure 7. The two rotation cases in question are labelled above each polar plot. The reflection model is specular and the object geometry is a cube.

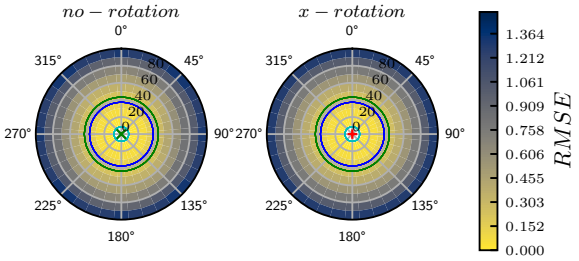

Fig. 9. Results for a diffuse reflection model and a icosahedron object geometry. RMSE is measured from a no-rotation no illumination offset baseline.

excluded because there was no discernible difference between those two plots and the two plots that have been provided. Figure 9 shows that the largest RMSEs were caused by increasing the phase angle, ϕ. All of the results appear to be independent of ψ angle. The four rotational motions cannot be distinguished from this figure.

In the pixel-to-pixel subtraction plots of Figure 10, the rotational motions are distinguishable. In Figure 10, the change in pixel values as ψ is varied shows that ψ does have an effect on the difference in RMSE. However, the magnitude of this difference is very small, which is shown by the scale bar having a maximum value of 0.05.

The much smaller RMSE measurements between the light curves of different rotational motions shows that the icosahedron with diffuse reflection has adopted a more ‘sphere-like’ behaviour. However as was the case for the previous results, the ideal conditions to distinguish these rotational motions is with maximum phase angle and an illumination vector closely aligned with the rotation vector.

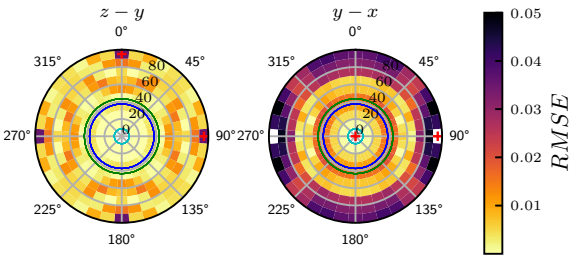

Fig. 10. The result of performing a pixel-to-pixel subtraction between two of the plots from Figure 9. The two rotation cases in question are labelled above each polar plot. The reflection model is diffuse and the object geometry is a icosahedron.

3.4. Icosahedron with specular reflection

The next two figures show the results for the icosahedron with a specular reflection model.

In Figure 11, increasing the phase angle is no longer the cause of the largest RMSE measurements. Instead, it is particular illumination vector directions that lead to these largest values, which is due to the high sensitivity of specular reflections to specific illumination conditions. In the no-rotation case, the large RMSE measurements at approximately $\phi = 60°$ and $\psi = 0°$ or $180°$ are caused by very bright specular reflections from a single facet of the icosahedron. In the rotating cases, the largest RMSE measurements were made when the illumination vector was placed such that bright specular glints were introduced into the light curve, that were not present in the baseline.

Figure 12 shows the pixel-to-pixel subtractions. The largest differences in the RMSE measurements shown in this plot result from illumination vector directions where specular glints are introduced into the light curves of one rotation state, but not the other.

These results exhibit a departure from the behaviour observed in previous figures. With specular reflection, the icosahedron geometry no longer demonstrates 'sphere-like' behaviour, as the measurable differences between rotational motions have greatly increased.

3.5. Polyhedron with diffuse reflection

The next two results are for the polyhedron, which was used to represent a sphere. Figure 13, once again, only shows the

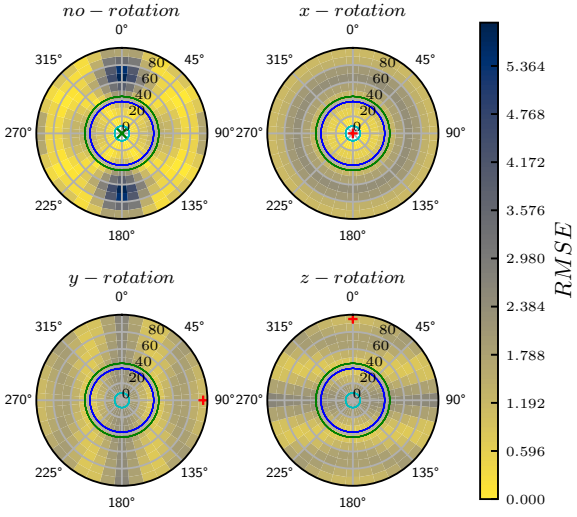

Fig. 11. Results for a specular reflection model and a icosahedron object geometry. RMSE is measured from a no-rotation no illumination offset baseline.

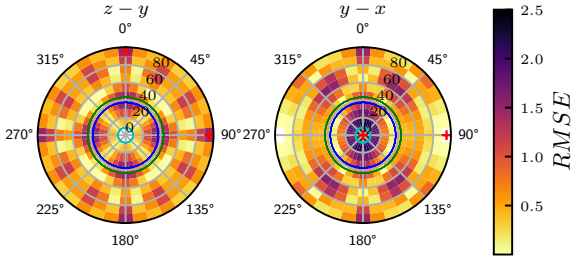

Fig. 12. The result of performing a pixel-to-pixel subtraction between two of the plots from Figure 11. The two rotation cases in question are labelled above each polar plot. The reflection model is specular and the object geometry is a icosahedron.

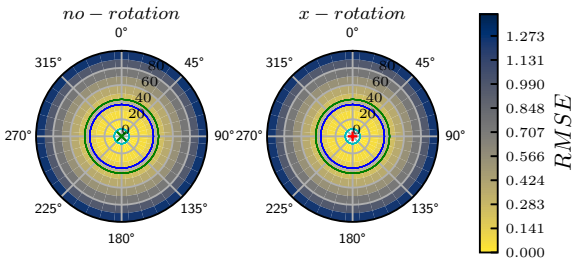

Fig. 13. Results for a diffuse reflection model and a 5-frequency subdivided polyhedron object geometry. RMSE is measured from a no-rotation no illumination offset baseline.

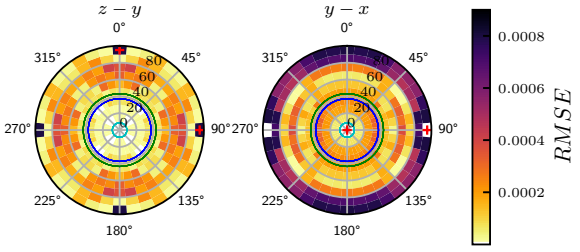

Fig. 14. The result of performing a subtraction between two of the plots from Figure 13. The two rotation cases in question are labelled above each polar plot. The reflection model is diffuse and the object geometry is a 5-frequency subdivided polyhedron.

no-rotation and x-rotation cases because the y-rotation and z-rotation cases are visually identical. In this figure, any changes in RMSE measurements due to the different rotation motions were negligible compared to brightness reduction due to increasing phase angle. This is the same result as the icosahedron geometry with a diffuse reflection model of Figure 9. This highlights the 'sphere-like' behaviour of icosahedron geometry under diffuse reflection conditions.

The subtraction plots are also very similar to those of the icosahedron with diffuse reflection, but the magnitude of the difference decreased by two orders of magnitude. The fact that differences are still measured between the different rotational motions is likely to be caused by the discretisation used to generate the object geometry. This again highlights the 'sphere-like' behaviour of the icosahedron with diffuse reflection.

3.6. Polyhedron with specular reflection

The next two figures present the results for the polyhedron with a specular reflection model. The polar plots of Figure 15 show all the same phenomena as the previous results. The only

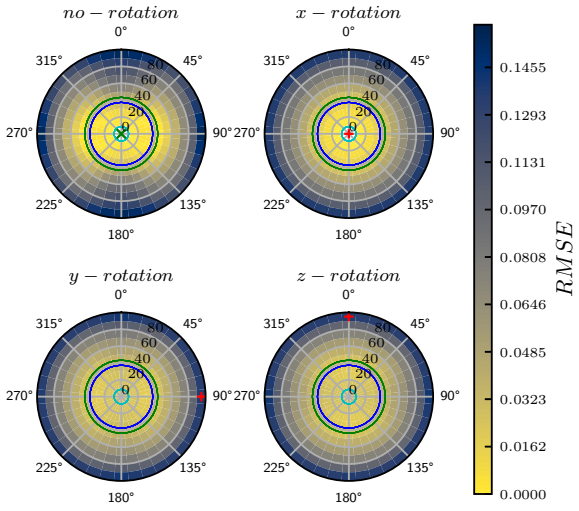

Fig. 15. Results for a specular reflection model and a 5-frequency subdivided polyhedron object geometry. RMSE is measured from a no-rotation no illumination offset baseline.

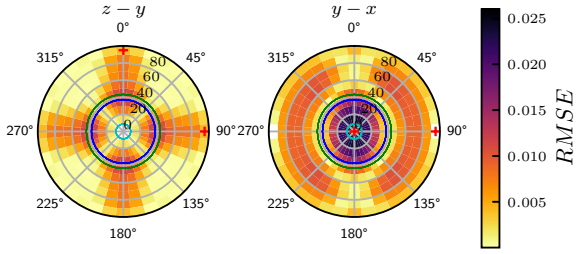

Fig. 16. The result of performing a subtraction between two of the plots from Figure 15. The two rotation cases in question are labelled above each polar plot. The reflection model is specular and the object geometry is a 5-frequency subdivided polyhedron

noticeable difference is a very slight ϕ angle dependence in the no-rotation case, which indicates that the polyhedron geometry is not perfectly isotropic. The fact that this result is so similar to the diffuse results shows that the polyhedron geometry is sufficiently spherical that strong specular reflections from single facets no longer have an effect on the light curves. This is in contrast to the icosahedron, which exhibited a breakdown in 'sphere-like' behaviour after switching to specular reflection.

The final subtraction plot is presented in Figure 16. The differences measured, which are larger than those for the diffuse case, are likely due to the object geometry discretisation and exacerbated by the specular reflection model.

3.7. Synthetic Light Curve Demonstration

To illustrate how the results presented in this paper may affect real-world light curve characterisation, a realistic demonstration light curve scenario was constructed. Like all previous synthetic light curves, the light curve was 240 s long and the object was placed at a fixed distance from the observer. This scenario used the cube geometry and a diffuse reflection model. Figure 17 shows the light curve illumination geometry at $t = 0$ and at $t = 240$. In this figure, all vectors lie in the plane of the x_b and y_b body-fixed rotation vectors, with the z_b vector pointing out of the page. This reference frame represents a satellite-centred orbital reference system for a circular orbit, where the X-axis points to the centre of the Earth, the Y-axis is coincident with the velocity vector and the Z-axis (out of the page) is the normal to the orbital plane. The body-fixed axes remain constant in this reference frame and so are therefore moving in the inertial frame. Throughout the light curve, the direction of the observation vector moved from the initial position shown on the left, to the final position shown on the right. This change in observation vector direction is equivalent to the observation vector motion that results from a satellite passing over a ground-based observation site. As a result of this motion, the phase angle increases from 40° at the start of the light curve to 80° at the end.

Figure 18 shows the light curves of the four considered rotational motions for this scenario. Two results are demonstrated in this plot. Firstly, only the z-rotation case shows a difference from the no-rotating case. The no-rotation, x-rotation and y-rotation cases are indistinguishable under these illumination conditions. These three light curves are superimposed in Figure 18. The second result is that the measurable difference between the z-rotation case and no-rotation case increased as phase angle increased. These light curves demonstrate the results of Figure 6, which showed that only a z-rotation is detectable if the observation vector, illumination vector and rotation vector are in the same plane.

A second light curve scenario was generated using a different object attitude state such that none of the three body-fixed

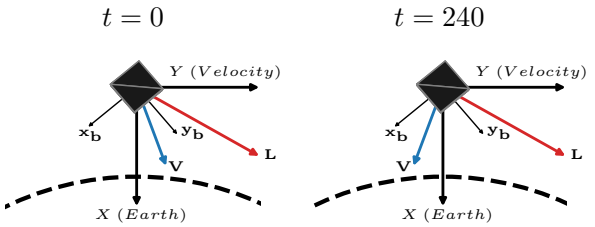

Fig. 17. The initial and final illumination conditions used in the first light curve scenario. **L** is the illumination vector and **V** is the observation vector. The curved dotted line shows the outline of the Earth.

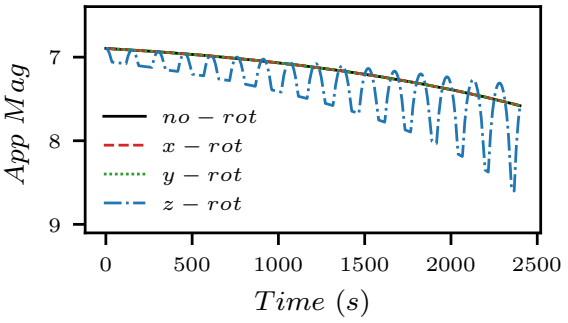

Fig. 18. Light curves for the four rotation states considered in this paper, using the illumination geometry presented in Figure 17. All light curves, with the exception of the 'z-rot' case are superimposed.

geometry axes were in the same plane as the observation and illumination vectors. This illumination geometry is shown in Figure 19. The only change from the previous scenario is the object's attitude state. Considering the light curves in Figure 20, the four rotational motions can now be distinguished, as the rotation axes are no-longer in the same plane as the observation and illumination vectors.

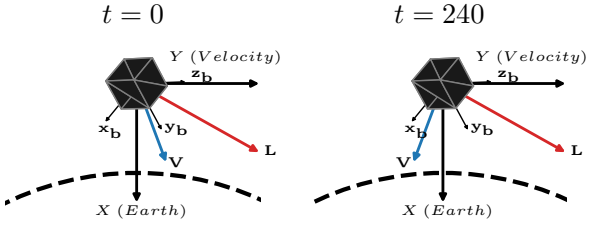

Fig. 19. The initial and final illumination conditions used in the first light curve scenario. **L** is the illumination vector and **V** is the observation vector. The curved dotted line shows the outline of the Earth.

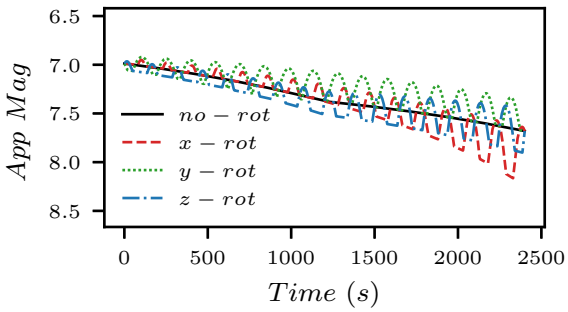

Fig. 20. Light curves for the four rotation states considered in this paper, using the illumination geometry presented in Figure 19.

4. Conclusions

The results presented in this work have demonstrated that the direction of the illumination vector with respect to the observation and rotation vectors can determine whether or not differences can be measured between light curves with different rotational motions.

In the results that used a diffuse reflection model, the most important parameter was phase angle and large phase angles were best able to distinguish between rotational motions. At low phase angles, the light curves of different rotational motions were either very similar or identical. Fortunately, if using ground-based observations of RSO's, very low phase angles are made impossible by the position of the Earth. However, this would be an important consideration for space-based observations as, typically, low phase angles are desired to maximise signal. When phase angle was sufficiently high, the direction of the illumination vector with respect to the axis of rotation became the most important parameter determining the measurable difference between rotational motions. No single illumination vector direction with respect to rotation vector was ideal for distinguishing all of the different rotational motions for each of the three object geometries. However, in all cases the ideal direction was either closely aligned with the rotation axis, or offset from it by 90°.

In the results using a specular reflection model, the direction of the illumination vector with respect to the object geometry had a much larger affect on the differences measured between rotational motions. This is particularly true for object geometries that have facets at a range of different angles such as the icosahedron. However, this result breaks down as the object becomes more spherical causing the specular results to become more similar to those for diffuse reflection.

Regardless of object geometry, attitude state and reflection model, the largest differences between rotations were measured with an illumination vector either closely aligned with the rotation axis, or offset from the rotation axis by 90°.

The results in this paper have identified illumination conditions that produce the largest measurable differences between different rotational motions. Certain properties can be generalised across the considered geometries and rotational motions. For example, a large phase angle typically increased the measurable differences. However, there was no single set of illumination conditions that provided large measurable differences between all the considered rotation motions for all geometries. Rather, the ideal conditions were specific to the object's shape, the reflection characteristics of its surfaces and the rotational motion to be detected. Furthermore, all results showed particular illumination conditions that resulted in only very small measurable differences between rotation motions.

This work indicates that characterising the rotational motion of an object from its brightness data is best performed using multiple observations. These observations should be constructed in such a way that maximises the difference in the illumination geometry. One way of achieving this would be by using observations from multiple observatories with a diverse range of geographical locations. This would maximise the measurable differences between rotation motions and minimise the possibility of incorrect characterisation.

5. Acknowledgements

This work was supported by the Engineering and Physical Sciences Research Council (Grant number EP/N509747/1) and grant PID2020-112576GB-C22 (MINECO/AEI/FEDER, UE).

References

Cook, R., & Torrance, K. (1982). A Reflectance Model for Computer Graphics. *ACM SIGGRAPH Computer Graphics*, *15*(3), 307–316. doi:10.1145/965161.806819.

Earl, M. A., & Wade, G. A. (2015). Observations of the Spin-Period Variations of Inactive Box-Wing Geosynchronous Satellites. *Journal of Spacecraft and Rockets*, *52*(3), 968–977. URL: http://arc.aiaa.org/doi/10.2514/1.A33077. doi:10.2514/1.A33077.

Goguen, J., Veverka, J., Elliot, J. L., & Church, C. (1976). The lightcurve and rotation period of asteroid 139 Juewa. *Icarus*, *29*(1), 137–142. URL: http://www.sciencedirect.com/science/article/pii/0019103576901081. doi:https://doi.org/10.1016/0019-1035(76)90108-1.

Kaasalainen, M., Lamberg, L., & Lumme, K. (1992a). Interpretation of lightcurves of atmosphereless bodies. II - Practical aspects of inversion. *Astronomy and Astrophysics*, *259*, 333–340. URL: https://ui.adsabs.harvard.edu/abs/1992A{&}A...259..333K.

Kaasalainen, M., Lamberg, L., Lumme, K., & Bowell, E. (1992b). Interpretation of lightcurves of atmosphereless bodies. I - General theory and new inversion schemes. *Astronomy and Astrophysics*, *259*, 318–332. URL: https://ui.adsabs.harvard.edu/abs/1992A{&}A...259..318K.

Kaasalainen, M., & Torppa, J. (2001). Optimization Methods for Asteroid Lightcurve Inversion: I. Shape Determination. *Icarus*, *153*(1), 24–36. URL: http://www.sciencedirect.com/science/article/pii/S0019103501966734. doi:https://doi.org/10.1006/icar.2001.6673.

Kaasalainen, M., Torppa, J., & Muinonen, K. (2001). Optimization Methods for Asteroid Lightcurve Inversion: II. The Complete Inverse Problem. *Icarus*, *153*(1), 37–51. URL: http://www.sciencedirect.com/science/article/pii/S0019103501966746. doi:https://doi.org/10.1006/icar.2001.6674.

Koshkin, N., Korobeynikova, E., Shakun, L., Strakhova, S., & Tang, Z. H. (2016). Remote Sensing of the EnviSat and Cbers-2B satellites rotation around the centre of mass by photometry. *Advances in Space Research*, *58*(3), 358–371. URL: http://dx.doi.org/10.1016/j.asr.2016.04.024. doi:10.1016/j.asr.2016.04.024.

Kutner, M. L. (2003). *Astronomy: A Physical Perspective*. (2nd ed.). Cambridge University Press‘. doi:https://doi.org/10.1017/CBO9780511802195.

Lewis, H. G., Swinerd, G. G., Newland, R. J., & Saunders, A. (2009). Active removal study for on-orbit debris using DAMAGE. *Fifth European Conference on Space Debris (02/04/09)*, *672 SP*(April). URL: https://eprints.soton.ac.uk/68969/.

Linares, R., Jah, M. K., Crassidis, J. L., & Nebelecky, C. K. (2014). Space Object Shape Characterization and Tracking Using Light Curve and Angles Data. *Journal of Guidance, Control, and Dynamics*, *37*(1), 13–25. URL: http://arc.aiaa.org/doi/abs/10.2514/1.62986. doi:10.2514/1.62986.

Liou, J.-C., & Johnson, N. L. (2008). Instability of the present LEO satellite populations. *Advances in Space Research*, *41*(7), 1046–1053. URL: http://www.sciencedirect.com/science/article/pii/S0273117707004097. doi:https://doi.org/10.1016/j.asr.2007.04.081.

Liou, J.-C., & Johnson, N. L. (2009). A sensitivity study of the effectiveness of active debris removal in LEO. *Acta Astronautica*, *64*(2), 236–243. URL: http://www.sciencedirect.com/science/article/pii/S0094576508002634. doi:https://doi.org/10.1016/j.actaastro.2008.07.009.

Liou, J.-C., Kieffer, M., Drew, A., & Sweet, A. (2020). Project Review. *Orbital Debris Quarterly News*, *24*(1), 4–8.

Schildknecht, T. (2007). Optical surveys for space debris. *The Astronomy and Astrophysics Review*, *14*(1), 41–111. URL: https://doi.org/10.1007/s00159-006-0003-9. doi:10.1007/s00159-006-0003-9.

Šilha, J., Pittet, J.-N., Hamara, M., & Schildknecht, T. (2018). Apparent rotation properties of space debris extracted from photometric measurements. *Advances in Space Research*, *61*(3), 844–861. URL: http://www.sciencedirect.com/science/article/pii/S027311771730786X. doi:https://doi.org/10.1016/j.asr.2017.10.048.

Torppa, J., Kaasalainen, M., Michałowski, T., Kwiatkowski, T., Kryszczyńska, A., Denchev, P., & Kowalski, R. (2003). Shapes and rotational properties of thirty asteroids from photometric data. *Icarus*, *164*(2), 346–383. URL: http://www.sciencedirect.com/science/article/pii/S0019103503001465. doi:https://doi.org/10.1016/S0019-1035(03)00146-5.

Wetterer, C. J., & Jah, M. K. (2009). Attitude Determination from Light Curves. *Journal of Guidance, Control, and Dynamics*, *32*(5), 1648–1651. URL: http://arc.aiaa.org/doi/abs/10.2514/1.44254. doi:10.2514/1.44254.

Williams, V. (1979a). Location of the rotation axis of a tumbling cylindrical earth satellite by using visual observations. Part I: Theory. *Planetary and Space Science*, *27*(6), 885–890. URL: http://www.sciencedirect.com/science/article/pii/003206337990014X. doi:10.1016/0032-0633(79)90014-X.

Williams, V. (1979b). Location of the rotation axis of a tumbling cylindrical earth satellite by using visual observations: Part II: Results. *Planetary and Space Science*, *27*(6), 891–894. URL: http://www.sciencedirect.com/science/article/pii/0032063379900151. doi:https://doi.org/10.1016/0032-0633(79)90015-1.